

Beyond Pixels: Medical Image Quality Assessment with Implicit Neural Representations

Caner Özer^{1,2}, Patryk Rygiel², Bram de Wilde², İlkay Öksüz¹, and Jelmer M. Wolterink²

¹ Computer Engineering Department, Istanbul Technical University, 34467 Maslak, Istanbul, Türkiye {ozerc}[at]itu.edu.tr

² Department of Applied Mathematics, Technical Medical Centre, University of Twente, Enschede, 7522 NB, The Netherlands

Abstract. Artifacts pose a significant challenge in medical imaging, impacting diagnostic accuracy and downstream analysis. While image-based approaches for detecting artifacts can be effective, they often rely on preprocessing methods that can lead to information loss and high-memory-demand medical images, thereby limiting the scalability of classification models. In this work, we propose the use of implicit neural representations (INRs) for image quality assessment. INRs provide a compact and continuous representation of medical images, naturally handling variations in resolution and image size while reducing memory overhead. We develop deep weight space networks, graph neural networks, and relational attention transformers that operate on INRs to achieve image quality assessment. Our method is evaluated on the ACDC dataset with synthetically generated artifact patterns, demonstrating its effectiveness in assessing image quality while achieving similar performance with fewer parameters.

Keywords: Medical Image Quality Assessment · Neural Fields · Artifact Detection · Implicit Neural Representations

1 Introduction

Artifacts in cardiac magnetic resonance imaging (MRI) [7] remain a persistent challenge, degrading diagnostic accuracy and complicating automated analysis. In cine MRI, artifacts typically arise from patient or respiratory motion [21], poor ECG triggering [13,16], or pacemakers [20]. Conventional image-based artifact detection methods [15,11], which are often heuristic-driven and parameter-heavy, struggle with scalability and consistency across different datasets.

Implicit neural representations (INRs) offer a promising alternative to commonly used voxel representations, providing compact, continuous signal representations that reduce memory demands while preserving essential details. INRs have shown success in tasks like periodic motion estimation [8], cardiac segmentation [1], and CT registration [22]. Moreover, INRs have been widely used in

MRI reconstruction, e.g. [4]. This results in images that are represented in an INR. However, it’s unclear how the quality of such an image can be directly assessed without having to resort to voxelization.

Clinically, distinguishing between moderate and severe artifacts is crucial, as these have the most significant impact on diagnostic reliability [12]. Motivated by this, we develop a framework to detect mild and severe artifacts in cine cardiac MRI represented as INRs. We address the computational burden of INR optimization [17] by introducing a parallel parameterization strategy that improves GPU efficiency. Our approach uniquely classifies artifact severity directly from INR parameters, combining parallel INR synthesis with weight-space classification, and represents, to our knowledge, the first such effort in medical image quality assessment.

2 Methods

In this section, we present our methodology for quality assessment. As shown in Figure 1, it consists of two stages. In Stage 1 (INR Construction), SIREN-based INRs are fitted to 2D slices of 3D+T cardiac MR images to encode them in weight space. This mimics the acquisition and direction reconstruction of MRI images to an INR. In Stage 2 (Classifier Training), these weights are used to train a classifier to predict image quality.

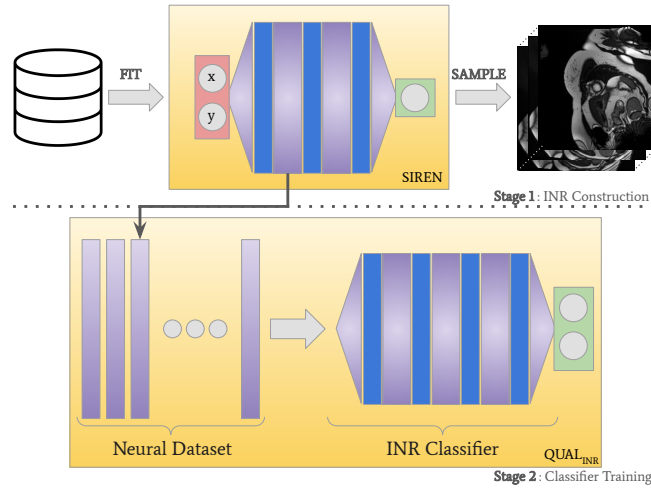


Fig. 1: INR construction and weight space training for classifying good and mid/poor quality acquisitions. In Stage 1, 2D slices from cardiac MR volumes in the dataset are fitted into INRs, which can then be used to reconstruct the 2D image slices via sampling. In Stage 2, the parameters of these INRs are used for training and prediction without sampling the 2D image slices.

2.1 Synthetic Mistriggering Artifact Generation Method

We generate synthetic artifacts by modifying the k-space representation of cine sequences, swapping frequencies between adjacent cardiac phases. The proportion of swapped frequencies is controlled by a hyperparameter P , called the corruption ratio. Higher P values lead to more pronounced mistriggering artifacts. We work with $2D + t$ image slices extracted from a specific depth of a $3D + t$ CMRI volume.

Let N denote the number of frequencies in an image slice and T the total number of adjacent slices. Given a $2D+time$ patient image, I , Algorithm 1 outlines the pseudocode for generating k-space-based mistriggering artifacts.

First, the algorithm computes the total number of frequencies to alter, n' , and randomly selects n' frequencies from a uniform distribution over $[0, N - 1]$. It also constructs a discrete reciprocal normal distribution over $[0, T - 1]$ centered on the current time-slice t , to ensure source frames differ from t . Finally, the selected k-space lines are copied from these source time-frames to the target.

Algorithm 1: k-space based randomized mistriggering artifact generation procedure

Result: I' , Images with mistriggering artifact
 $I, N, T, P, t, t', n', I'$
while $t \leq T - 1$ **do**
 $n' := NP$
 select random n' lines from a Uniform distribution
 form a discrete reciprocal Normal distribution
 select random t' lines from that distribution
 apply changes on I' using I, n' and t'
 $t := t + 1$
end

To generate images of varying quality, we set $P = 0.05$ for mid-quality and $P = 0.15$, for poor-quality images.

2.2 Stage 1: INR Generation

Given that we have good, mid, and poor-quality cardiac MRI acquisitions after applying our synthetic artifact generation method, we synthesize implicit neural representations (INRs) corresponding to the 2D slices present in these acquisitions. Formally, let us denote the set of all 2D images as signals $\{s_1, s_2, \dots, s_N\}$. For each signal s_i , the coordinates $\mathbf{x}_j \in \mathbb{R}^2$ and corresponding pixel intensity values $y_j \in \mathbb{R}$ are available, with a total of M such coordinate-intensity pairs. The mapping $f_{\theta_i} : \mathbb{R}^2 \rightarrow \mathbb{R}$ aims to model this relationship by optimizing the parameters θ_i for each signal s_i .

We apply an L -layer MLP architecture with a hidden dimension of D and sinusoidal activations of SIREN [19], where the INR model is represented as:

$$f_{\theta_i}(\mathbf{x}) = \mathbf{W}_{l-1}(\phi_{l-2} \circ \phi_{l-3} \circ \dots \circ \phi_0) + \mathbf{b}_{l-1}, \quad \phi_l(\mathbf{x}_i) = \sin(\omega_0(\mathbf{W}_l \mathbf{x}_i + \mathbf{b}_l)) \quad (1)$$

where \mathbf{W}_i and \mathbf{b}_i are the learnable parameters of the i -th layer, and ω_0 is a hyperparameter that controls the spatial frequency. Following [17], we apply a fixed initialization with a single seed across all f_{θ_i} 's.

To optimize the parameters of f_{θ_i} , we define a loss function that minimizes the squared error between the sampled and actual pixel intensity values for all available coordinate-intensity pairs:

$$\mathcal{L} = \frac{1}{M} \sum_j \|y_j - f_{\theta_i}(\mathbf{x}_j)\|^2. \quad (2)$$

Since sequential optimization would take weeks with 2,000 iterations per INR, we parallelize using JAX (v0.4.23) [3] with vectorized mapping, fitting up to 400 INRs at a time on four NVIDIA PASCAL GPUs to fully utilize VRAM.

Overall, the SIREN-based network effectively models the quality of good-, mid-, and poor-quality images. We perform this fitting for all 2D slices, building a neural dataset from the INR parameters³.

2.3 Stage 2: INR Classification

This section details the INR classification after constructing the neural dataset. To preserve efficiency in terms of parameter utilization, we do not sample the image for classification purposes; instead, we work directly with the learned parameters of the INRs.

To evaluate different modeling strategies for INR classification, we assess four architectures: multi-layer perceptron (MLP), deep weight space networks (DWSNets) [14], graph neural networks (GNNs) [9,5], and relational attention transformers [9,6]. Each of these architectures provides a unique perspective on learning representations from INR parameters. The MLP serves as a baseline approach, where the flattened INR parameters are treated as a high-dimensional input vector. DWSNets introduce equivariant layers that exploit the relational structure among INR weights and biases. GNNs are employed under the hypothesis that INR parameter structures exhibit relational properties, where connections between layers can be exploited to improve classification when represented as a graph. In this formulation, biases of INRs are encoded as node features, while weights act as edge features. Finally, relational transformers leverage the same structural property while aiming to model higher-order dependencies within INR weight distributions, capturing long-range interactions that may be overlooked by conventional architectures.

MLP: The MLP consists of four hidden layers, each with 64 dimensions. The output of each layer is passed through a 1D batch normalization layer followed by ReLU activations. A final output layer completes the classification process.

³ <https://github.com/canerozer/fit-a-nef/>

DWSNets: The DWSNet implementation follows [14], incorporating four equivariant layers with 64 dimensions, along with a final invariant layer responsible for flattening, max-reduction, and prediction operations.⁴

GNN: The GNN model is adopted from [9], utilizing four message-passing layers, each with a hidden size of 32. Additionally, 32-dimensional probing features are incorporated to augment the node representations.⁵

Transformer: The transformer model is based on [9], employing four attention layers with eight heads per layer, while other hyperparameters remain unchanged. Similar to the GNN, the transformer architecture also benefits from the probing mechanism, enhancing feature representation and learning.⁵

The classification tasks are divided into two separate evaluations: *Good vs. Poor* and *Good vs. Mid*. Both tasks involve predicting the quality category of an MRI slice based on the INR parameters learned during Stage 1. Given that these quality labels originate from controlled synthetic artifact generation, the classifier aims to identify INR-specific patterns that correspond to these predefined categories. We adopt binary cross-entropy loss as the optimization objective and use AdamW to optimize the model parameters. All of these models were implemented in PyTorch (v2.0.1).

To prevent overfitting [18] and improve generalization, we apply standard regularization techniques, including dropout (0.2, except for MLP), weight decay (0.0005), and data augmentation strategies such as rotation, noise injection, and scaling. Additionally, we employ early stopping based on validation accuracy, training the networks for a maximum of 10 epochs. The learning rate is set to 0.0005 for MLP and DWSNet, 0.001 for GNN and Transformer.

3 Experimental Results

In this section, we describe the dataset and present the experimental results of the classifiers. We evaluate the performance using classification accuracy for both the Good vs. Poor and Good vs. Mid tracks, repeating all experiments 10 times with different seed values. We will make the code available upon the acceptance of the paper.

Dataset: We present our results using the ACDC Challenge dataset [2], which comprises 150 3D+t short-axis Cardiac MR acquisitions. These acquisitions are evenly distributed across five cardiac conditions: normal, heart failure with infarction, dilated cardiomyopathy, hypertrophic cardiomyopathy, and abnormal right ventricle. To maintain a balanced representation, we allocate 90 acquisitions for training, 10 for validation, and 50 for testing. Synthetic artifacts are introduced following this distribution. During neural dataset construction, we apply center crops of 256×256 while ensuring that essential cardiac structures remain visible. After constructing the neural dataset, the sample distribution per quality label (good, mid, and poor) is as follows: 22,749 for training, 2,602 for validation, and 12,995 for testing. Also, setting the number of layers, $L = 3$, and

⁴ <https://github.com/canerozer/DWSNets>

⁵ <https://github.com/canerozer/NeuralGraphs>

their hidden dimension to 64 allowing us to represent a signal with 14.8 times fewer parameters considering a reduction from 65,536 to 4,417.

3.1 Image Quality vs. INR Classification

Figure 2 presents the classification accuracy as a function of PSNR, where PSNR values are obtained through early stopping during INR optimization. This is done by defining multiple PSNR threshold values and halting INR parameter optimization once the corresponding threshold is reached. To see this effect of early stopping qualitatively, Figure 3 underscores this by illustrating how the reconstructed signals qualitatively vary across different average PSNR levels after early stopping, providing visual examples that complement the quantitative accuracy trends in Figure 2.

We observe that the accuracy for Good vs. Poor remains relatively stable across PSNR levels but shows an upward trend at higher PSNR values, indicating that improved INR reconstructions enhance classification reliability. In contrast, Good vs. Mid classification exhibits slightly more fluctuations, with accuracy decreasing at intermediate PSNR values before improving at higher PSNR levels.

The best classification performance is observed at a PSNR of 29.85 dB, where accuracy reaches 0.918 for Good vs. Poor and 0.804 for Good vs. Mid. However, when training continues for 2,000 iterations, resulting in an average PSNR of 31.07 dB, accuracy slightly decreases to 0.904 for Good vs. Poor and 0.787 for Good vs. Mid. This suggests that while improving INR reconstruction quality generally enhances classification, excessive training may introduce minor degradation in performance. Overall, the trend indicates that higher PSNR, achieved through better INR optimization, contributes to improved classification accuracy, particularly for the Good vs. Poor task.

An interesting observation from this plot is that an average reconstruction quality of 14.97 dB of PSNR is achieved after just a single iteration, while still obtaining an average accuracy of 0.9081 for Good vs. Poor and 0.7721 for Good vs. Mid. This suggests that even the early-stage INR parameters provide predictive information to enable classification to some extent. We focus on converged INR parameters, as they are likely to be more informative for applications beyond classification.

3.2 Image Quality Assessment Performance

In Table 1, we present the results of the test splits. The first row corresponds to image-based classification using a pixel-based MLP classifier operating on flattened pixel intensities, with over 12 million parameters due to the input resolution of 256×256 . Despite its high parameter count, the pixel-based MLP underperforms compared to INR-based methods, achieving only 0.727 and 0.529 accuracy for the Good vs. Poor and Good vs. Mid tasks, respectively. This performance gap suggests that flattened pixel intensities alone may not sufficiently capture essential spatial patterns indicative of image quality, highlighting the need for more effective representations.

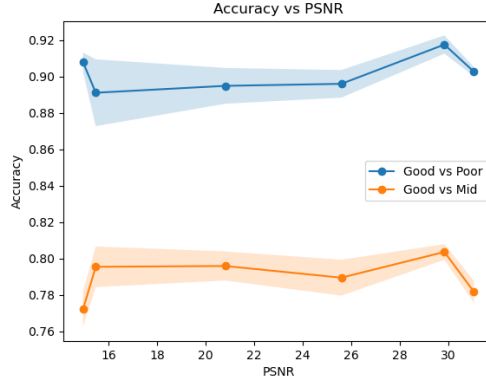


Fig. 2: Relationship between reconstruction quality (PSNR) and INR classification performance for the MLP model. Each point shows the average classification accuracy at a PSNR threshold, with shaded standard deviation.

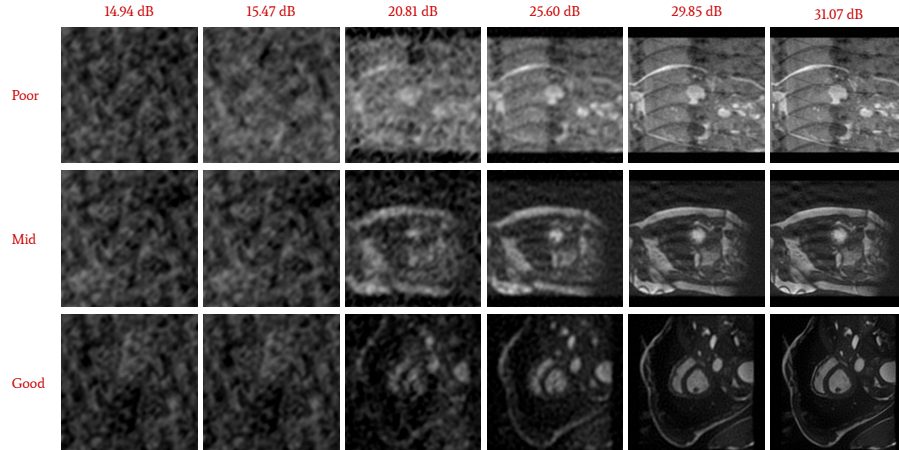


Fig. 3: Signal reconstructions from various INRs trained on neural datasets with different average reconstruction PSNRs after early stopping.

Among the INR-based methods, the Transformer (Probe=32) model achieves the highest performance, with classification accuracies of 0.944 and 0.833 on the Good vs. Poor and Good vs. Mid tasks, respectively, while using significantly fewer parameters than the image-based MLP model. Notably, even the INR-based MLP model achieves accuracies of 0.904 and 0.787 for the same tasks. These results highlight both the effectiveness of lightweight architectures operating in INR weight space and the benefits of probe-based mechanisms. Furthermore, the superior performance of the Transformer (Probe=32) model is statistically significant compared to other models, with a p-value < 0.01 .

Model Name	Number of Parameters	Good vs. Poor	Good vs. Mid
Image-Based Model (MLP)	12.6M	0.727	0.529
MLP	300K	0.904	0.787
DWSNet	2.16M	0.901	0.770
GNN	96K	0.929	0.808
Transformer	376K	0.933	0.816
GNN (Probe=32)	96K	0.938	0.817
Transformer (Probe=32)	384K	0.944	0.833

Table 1: Performance comparison of various image-based and INR-based models on the "Good vs. Poor" and "Good vs. Mid" quality classification.

4 Conclusion & Discussion

This study introduced an INR-based framework for medical image quality assessment, leveraging neural fields to efficiently classify mistriggering artifacts in cardiac MRI. By directly using INR parameters, our method reduces memory and computational overhead compared to traditional image-based approaches, while maintaining high accuracy. Parallelized INR optimization further supports scalability across large datasets.

Our experiments in the ACDC dataset demonstrated that INR-based classification achieves improved accuracy compared to the image-based MLP model, with the Transformer (Probe=32) achieving 94.4% (Good vs. Poor) and 83.3% (Good vs. Mid) accuracy. We also notice that classification performance improved with INR reconstruction quality, peaking at 29.85 dB PSNR, though even early-stage INR optimization retained strong predictive power. These findings highlight the potential of INR parameters as meaningful descriptors of image quality, supporting the feasibility of neural fields for artifact detection.

Limitations include the computational cost of INR optimization, even in parallel, and the restricted variability of synthetic artifacts, which may not fully reflect real-world cases. Broader validation on datasets like CMRxMotion [21] and LDCTIQAC [10] is left for future work.

Overall, our approach demonstrates a promising, lightweight alternative to large CNN-based models for scalable artifact detection. Future directions include improving INR optimization speed for real-time use, broader dataset validation, and exploring INR editing [23] for artifact correction to further support clinical decision-making.

Acknowledgement. This work has been benefitted from the 2232 International Fellowship for Outstanding Researchers Program of TUBITAK (Project No: 118C353). However, the entire responsibility of the thesis belongs to the owner. The financial support received from TUBITAK does not mean that the content of the thesis is approved in a scientific sense by TUBITAK. This work was supported by Scientific Research Projects Department of Istanbul Technical University. Project Numbers: 44250 and 47296.

References

1. Ansó, N.S., McGinnis, J., Pan, J., Hammernik, K., Rueckert, D.: NISF: neural implicit segmentation functions. In: Greenspan, H., Madabhushi, A., Mousavi, P., Salcudean, S.E., Duncan, J., Syeda-Mahmood, T.F., Taylor, R.H. (eds.) Medical Image Computing and Computer Assisted Intervention - MICCAI 2023 - 26th International Conference, Vancouver, BC, Canada, October 8-12, 2023, Proceedings, Part IV. Lecture Notes in Computer Science, vol. 14223, pp. 734–744. Springer (2023). https://doi.org/10.1007/978-3-031-43901-8_70
2. Bernard, O., Lalande, A., Zotti, C., Cervenansky, F., Yang, X., Heng, P.A., Cetin, I., Lekadir, K., Camara, O., Ballester, M.A.G., et al.: Deep learning techniques for automatic mri cardiac multi-structures segmentation and diagnosis: is the problem solved? *IEEE Transactions on Medical Imaging* **37**(11), 2514–2525 (2018)
3. Bradbury, J., Frostig, R., Hawkins, P., Johnson, M.J., Leary, C., Maclaurin, D., Necula, G., Paszke, A., VanderPlas, J., Wanderman-Milne, S., Zhang, Q.: JAX: composable transformations of Python+NumPy programs (2018), <http://github.com/google/jax>
4. Chu, J., Du, C., Lin, X., Zhang, X., Wang, L., Zhang, Y., Wei, H.: Highly accelerated MRI via implicit neural representation guided posterior sampling of diffusion models. *Medical Image Anal.* **100**, 103398 (2025), <https://doi.org/10.1016/j.media.2024.103398>
5. Corso, G., Cavalleri, L., Beaini, D., Liò, P., Velickovic, P.: Principal neighbourhood aggregation for graph nets. In: Larochelle, H., Ranzato, M., Hadsell, R., Balcan, M., Lin, H. (eds.) *Proc. NeurIPS* (2020)
6. Diao, C., Loynd, R.: Relational attention: Generalizing transformers for graph-structured tasks. In: The Eleventh International Conference on Learning Representations, ICLR 2023, Kigali, Rwanda, May 1-5, 2023 (2023), <https://openreview.net/forum?id=cFuMmbWiN6>
7. Ferreira, P.F., Gatehouse, P.D., Mohiaddin, R.H., Firmin, D.N.: Cardiovascular magnetic resonance artefacts. *JCMR* **15**(1), 41 (May 2013)
8. Garzia, S., Rygiel, P., Dummer, S., Cademartiri, F., Celi, S., Wolterink, J.M.: Neural fields for continuous periodic motion estimation in 4d cardiovascular imaging. In: *International Workshop on Statistical Atlases and Computational Models of the Heart*. pp. 378–389. Springer (2024)

9. Kofinas, M., Knyazev, B., Zhang, Y., Chen, Y., Burghouts, G.J., Gavves, E., Snoek, C.G.M., Zhang, D.W.: Graph neural networks for learning equivariant representations of neural networks. In: The Twelfth International Conference on Learning Representations, ICLR 2024, Vienna, Austria, May 7-11, 2024 (2024), <https://openreview.net/forum?id=o06FsMyDBt>
10. Lee, W., Wagner, F., Galdran, A., Shi, Y., Xia, W., Wang, G., Mou, X., Ahamed, M.A., Imran, A.A.Z., Oh, J.E., Kim, K., Baek, J.T., Lee, D., Hong, B., Tempelman, P., Lyu, D., Kuiper, A., van Blokland, L., Calisto, M.B., Hsieh, S., Han, M., Baek, J., Maier, A., Wang, A., Gold, G.E., Choi, J.H.: Low-dose computed tomography perceptual image quality assessment. *Medical Image Analysis* **99**, 103343 (2025). <https://doi.org/https://doi.org/10.1016/j.media.2024.103343>
11. Lei, K., Syed, A.B., Zhu, X., Pauly, J.M., Vasanawala, S.S.: Artifact- and content-specific quality assessment for mri with image rulers. *Medical Image Analysis* **77**, 102344 (2022). <https://doi.org/https://doi.org/10.1016/j.media.2021.102344>
12. Loizillon, S., Bottani, S., Maire, A., Ströer, S., Dormont, D., Colliot, O., Burgos, N.: Automatic motion artefact detection in brain t1-weighted magnetic resonance images from a clinical data warehouse using synthetic data. *Medical Image Analysis* **93**, 103073 (2024). <https://doi.org/https://doi.org/10.1016/j.media.2023.103073>
13. Lyu, Q., Shan, H., Xie, Y., Kwan, A.C., Otaki, Y., Kuronuma, K., Li, D., Wang, G.: Cine cardiac mri motion artifact reduction using a recurrent neural network. *IEEE Transactions on Medical Imaging* **40**(8), 2170–2181 (2021). <https://doi.org/10.1109/TMI.2021.3073381>
14. Navon, A., Shamsian, A., Achituve, I., Fetaya, E., Chechik, G., Maron, H.: Equivariant architectures for learning in deep weight spaces. In: Krause, A., Brunskill, E., Cho, K., Engelhardt, B., Sabato, S., Scarlett, J. (eds.) *Proc. ICML*. vol. 202, pp. 25790–25816 (23–29 Jul 2023), <https://proceedings.mlr.press/v202/navon23a.html>
15. Oksuz, I., Ruijsink, B., Puyol-Antón, E., Clough, J.R., Cruz, G., Bustin, A., Prieto, C., Botnar, R., Rueckert, D., Schnabel, J.A., King, A.P.: Automatic cnn-based detection of cardiac mr motion artefacts using k-space data augmentation and curriculum learning. *Medical Image Analysis* **55**, 136–147 (2019). <https://doi.org/https://doi.org/10.1016/j.media.2019.04.009>
16. Özer, C., Öksüz, İ.: Cross-domain artefact correction of cardiac mri. In: Puyol Antón, E., Pop, M., Martín-Isla, C., Sermesant, M., Suinesiaputra, A., Camara, O., Lekadir, K., Young, A. (eds.) *Statistical Atlases and Computational Models of the Heart. Multi-Disease, Multi-View, and Multi-Center Right Ventricular Segmentation in Cardiac MRI Challenge*. pp. 199–207. Springer International Publishing, Cham (2022)
17. Papa, S., Valperga, R., Knigge, D.M., Kofinas, M., Lippe, P., Sonke, J., Gavves, E.: How to train neural field representations: A comprehensive study and benchmark. In: *Proc. IEEE CVPR*. pp. 22616–22625 (2024), <https://doi.org/10.1109/CVPR52733.2024.02134>
18. Shamsian, A., Zhang, D.W., Navon, A., Zhang, Y., Kofinas, M., Achituve, I., Valperga, R., Burghouts, G.J., Gavves, E., Snoek, C.G.M., Fetaya, E., Chechik, G., Maron, H.: Data augmentations in deep weight spaces (2023), <https://arxiv.org/abs/2311.08851>
19. Sitzmann, V., Martel, J.N., Bergman, A.W., Lindell, D.B., Wetzstein, G.: Implicit neural representations with periodic activation functions. In: *Proc. NeurIPS* (2020)
20. Vuorinen, A.M., Lehmonen, L., Karvonen, J., Holmström, M., Kivistö, S., Kaasalainen, T.: Reducing cardiac implantable electronic device-induced artefacts

- in cardiac magnetic resonance imaging. *European Radiology* **33**(2), 1229–1242 (Feb 2023). <https://doi.org/10.1007/s00330-022-09059-w>
21. Wang, S., Qin, C., Wang, C., Wang, K., Wang, H., Chen, C., Ouyang, C., Kuang, X., Dai, C., Mo, Y., Shi, Z., Dai, C., Chen, X., Wang, H., Bai, W.: The extreme cardiac mri analysis challenge under respiratory motion (cmrxmotion) (2022), <https://arxiv.org/abs/2210.06385>
 22. Wolterink, J.M., Zwienenberg, J.C., Brune, C.: Implicit neural representations for deformable image registration. In: Konukoglu, E., Menze, B.H., Venkataraman, A., Baumgartner, C.F., Dou, Q., Albarqouni, S. (eds.) *International Conference on Medical Imaging with Deep Learning, MIDL 2022, 6-8 July 2022, Zurich, Switzerland. Proceedings of Machine Learning Research*, vol. 172, pp. 1349–1359. PMLR (2022), <https://proceedings.mlr.press/v172/wolterink22a.html>
 23. Zhou, A., Yang, K., Jiang, Y., Burns, K., Xu, W., Sokota, S., Kolter, J.Z., Finn, C.: Neural functional transformers. In: *Proc. NeurIPS* (2023)